Published in final edited form as:

Nat Neurosci. 2022 December ; 25(12): 1706–1713. doi:10.1038/s41593-022-01202-6.

Dual color mesoscopic imaging reveals spatiotemporally heterogeneous coordination of cholinergic and neocortical activity

Sweyta Lohani[1,*], **Andrew H. Moberly**[1,*], **Hadas Benisty**[1], **Boris Landa**[2], **Miao Jing**[3], **Yulong Li**[4], **Michael J. Higley**[1,#], **Jessica A. Cardin**[1,#]

[1]Department of Neuroscience, Kavli Institute for Neuroscience, Yale University School of Medicine, New Haven, CT 06510 USA

[2]Program in Applied Mathematics, Yale University, New Haven, CT 06510 USA

[3]Chinese Institute for Brain Research, Beijing, 102206, China

[4]State Key Laboratory of Membrane Biology, Peking University School of Life Sciences; PKU-IDG/McGovern Institute for Brain Research; Peking-Tsinghua Center for Life Sciences, Beijing 100871, China

Abstract

Variation in an animal's behavioral state is linked to fluctuations in brain activity and cognitive ability. In the neocortex, state-dependent control of circuit dynamics may reflect neuromodulatory influences including acetylcholine (ACh). While early literature suggested ACh exerts broad, homogeneous control over cortical function, recent evidence indicates potential anatomical and functional segregation of cholinergic signaling. Additionally, it is unclear whether states as defined by different behavioral markers reflect heterogeneous cholinergic and cortical network activity. We performed simultaneous, dual-color mesoscopic imaging of both ACh and calcium across the neocortex of awake mice to investigate their relationships with behavioral variables. We find that increasing arousal, categorized by different motor behaviors, is associated with spatiotemporally dynamic patterns of cholinergic modulation and enhanced large-scale network correlations. Overall, our findings demonstrate that ACh provides a highly dynamic and spatially heterogeneous signal that links fluctuations in behavior to functional reorganization of cortical networks.

[#]These authors share primary correspondence for this work. **Lead Contacts:** jess.cardin@yale.edu, m.higley@yale.edu.
[*]These authors contributed equally to this work.

Author Contributions

SL, AHM, MJ, YL, MJH, and JAC designed the experiments. SL and AHM collected the data. SL, AHM, HB, and BL analyzed the data. SL, AHM, MJH, and JAC wrote the manuscript.

Code Availability Statement

Custom written MATLAB scripts used in this study are available from the corresponding authors on reasonable request.

Conflicts of Interest

The authors declare no conflicts of interest exist.

Introduction

Animals cycle through multiple waking brain states that profoundly influence patterns of neuronal activity, perception, and behavior[1–4]. Waking states can be categorized by a variety of cognitive and motor variables, including pupil dilation, facial movement, locomotion, arousal, and attention [1, 5]. However, it is unclear whether variation in these parameters reflects different underlying brain network dynamics. A growing body of research suggests that arousal, measured using a variety of metrics including elevated motor activity, is associated with distinct alterations in local circuit operations within the neocortex, including changes in mean firing rates and decorrelation of the spike output of neighboring cells[3, 6–9]. Moreover, widefield, mesoscopic imaging[10] has revealed broad representation of motor signals across the cortex[8], with changes in behavioral state also linked to reorganization of functionally connected cortical networks[11, 12]. While desynchronization of local cortical network activity is a hallmark of transitions from periods of quiescence to periods of high arousal or motor output, it is unclear whether large-scale circuits spanning multiple cortical areas also exhibit changes in coordination across state transitions.

Classical views suggest that variation in neural activity associated with behavioral state fluctuations reflects the brain-wide, homogeneous influence of ascending neuromodulatory systems[13]. For example, cholinergic neurons in the basal forebrain send widespread projections throughout the neocortex that are thought to contribute to the effects of arousal, attention, and emotional valence on cortical dynamics[5, 14–19]. Application of ACh evokes desynchronization of local field potentials, de-correlates neuronal spiking, and enhances response gain, phenomena linked to enhanced attention and information representation[6, 19–28]. In addition, cholinergic neurons fire strongly to positive and negative reinforcement[29, 30], resulting in reinforcement-related plasticity in the cortex[15, 31]. These studies suggest that highly salient environmental stimuli may produce uniform ACh signaling across the cortex to enhance global information processing and plasticity. However, recent electrophysiological and anatomical studies indicate substantial diversity in the firing patterns and axonal arborizations of individual cholinergic neurons, suggesting their output may instead be spatially and temporally heterogeneous in different cortical areas[7, 32–35]. Furthermore, the spatiotemporal relationships between cholinergic signaling and cortical neuronal activity across distinct behavioral states are unknown.

Monitoring cholinergic activity *in vivo* has typically required invasive probes with limited spatiotemporal resolution[36]. However, the development of receptor-based fluorescent indicators that directly report ACh binding has opened new avenues for the exploration of neuromodulation. Here, we used two-color mesoscopic imaging[10] of the red-fluorescent calcium indicator jRCaMP1b[37] and the green-fluorescent ACh indicator ACh3.0[38] across the entire dorsal neocortex of the awake mouse to quantify the relationships between behavioral state, cortical activity, and cholinergic signaling. Our results demonstrate that, in contrast to traditional models, different behavioral states categorized by motor behavior are associated with distinct spatiotemporal patterns of ACh fluctuations and increased large-scale network synchronization. Moreover, pharmacological manipulation of muscarinic receptor activity produces spatially distinct alterations in cortical activity. Overall, these findings re-shape our view of neuromodulation from a global state variable to a highly

dynamic and spatially heterogeneous signal that links fluctuations in behavior to cortical network dynamics.

Results

Dual-color mesoscopic ACh and calcium imaging

To simultaneously monitor neuronal activity and cholinergic signaling in the neocortex of awake mice, we expressed the red fluorescent calcium indicator jRCaMP1b[37] and the green fluorescent ACh sensor ACh3.0[38] throughout the brain via neonatal injection of AAV vectors into the transverse sinus[11, 39]. This approach resulted in cortex-wide, uniform expression of both reporters (Figure S1), and we confirmed both *ex vivo* and *in vivo* that ACh3.0 specifically reported cholinergic signaling (Figure S2). We then performed mesoscopic imaging[10] of both reporters through the intact skull of mice that were head-fixed and freely running on a wheel (Figure 1a, see Methods). Imaging was performed by strobing 575nm (jRCaMP1b), 470nm (ACh3.0), and 395nm (control) excitation light with an overall frame rate of 10 Hz per channel. ACh3.0 and jRCaMP1b images were co-registered, aligned to the Allen Common Coordinate Framework (CCFv3, Figure S2)[40], and normalized ($\Delta F/F$). There was no observable cross-talk between the green (ACh3.0) and red (jRCaMP1b) channels (Figure S2). We removed hemodynamic and motion-related artifacts using a novel regression-based approach that leverages spatial correlations in signal and noise and takes advantage of the reduced ACh-sensitive fluorescence of ACh3.0 when excited at 395nm[38] (Figure S3, see Methods). This method outperformed conventional pixel-wise regression in its ability to remove stimulus-induced and spontaneous behavior-associated negative transients in fluorescence corresponding to hemodynamic absorption[41, 42] (Figure S3, S4).

Both ACh and calcium signals exhibited spatially heterogeneous, spontaneous fluctuations across the cortex (Figure 1b,c), illustrated by example data from two spatially distant cortical areas, primary visual (V1) and supplemental motor (M2) cortex. To investigate the relationship of this activity to behavior, we tracked the animal's state using a combination of variables thought to reflect, in different ways, the animal's overall level of arousal (Figure S5; Supplemental Table 1). Locomotion (wheel running speed) and pupil diameter have been repeatedly linked to variability in behavioral performance [4, 43–46] and are associated with distinct patterns of local circuit dynamics[1, 3, 8, 47]. In addition, facial movements like whisking, which reflects the animal's active exploration of its environment, are also[48] closely coupled to cortical function[7, 9, 49] and have been captured using FaceMap software to dimensionally reduce facial video data[9]. To complement imaging and behavioral data, we also recorded local circuit dynamics via electrocorticogram (ECoG) in a subset of experiments.

Overall, large fluorescence signal fluctuations occurred across cortical regions for both cholinergic and calcium signals and co-varied with changes in pupil dilation, locomotion, facial movement, and high-frequency ECoG activity (Figure 1c). Moreover, inter-areal correlations for both ACh and calcium were dynamic and tracked variation in behavioral variables [50]. Spatially varied activity patterns in both channels were evident during specific periods of arousal (Figure 1, highlighted time frames), supporting a model in which ACh release is both dynamic and heterogeneous across cortical regions.

Calcium and cholinergic signals encode behavioral state

To quantify the relationships between behavioral variables and fluorescence activity, we built cross-validated ridge regression models that included facial movements (FaceMap principal components 1–25, see Methods), locomotion speed, and pupil size as predictors of either ACh or calcium fluctuations for each CCFv3-defined parcel. For ACh3.0 and jRCaMp1b, the variance explained (R^2) using this full model differed significantly across cortical areas (Figure 2a,b, $p<0.001$ for Ach 3.0 and jRCaMp1b, Friedman's ANOVA, n = 6 mice per group). We also observed significant anterior-posterior gradients in the coupling between behavioral state and fluorescence activity that were inverted for cholinergic versus calcium signals (Figure 2b, Spearman's rank test), with ACh release and calcium signaling most strongly linked to behavioral state variables in frontal and posterior areas, respectively. To examine the relative relationships between each behavioral metric and neural activity, we first constructed a full model while temporally shuffling the data for one predictor and calculating the change in predictive power (ΔR^2), reflecting the unique contribution of the shuffled variable. We also constructed single predictor models to examine the ability of each individual variable to predict neural activity[8] (see Methods). For facial movements, we explicitly examined the contribution of the first FaceMap PC. For ACh3.0, both single variable and shuffled models produced similar results with significant differences between behavioral metrics ($p=0.006$ and $p=0.003$ for R^2 and ΔR^2, respectively, Friedman's ANOVA, n=6 mice per group). Facial movements yielded the strongest prediction accuracy compared to locomotion and pupil variation for Ach 3.0 (Figure 2c, S6; R^2: $p=0.031$ for face PC1 vs. locomotion, $p=0.031$ for face PC1 vs. pupil, $p=0.063$ for locomotion vs. pupil; ΔR^2: $p=0.031$ for face PC1 vs. locomotion, $p=0.031$ for face PC1 vs. pupil, $p=0.031$ for locomotion vs. pupil; post-hoc signed rank tests). For jRCaMP1b, both single predictor R^2 and ΔR^2 measures differed significantly by state ($p=0.006$ and $p=0.03$ for R^2 and ΔR^2, respectively, Friedman's ANOVA, n=6 mice per group). Again, facial movement (PC1) was the most robust predictor (Figure 2c, S6; R^2: $p=0.031$ for face vs. locomotion, $p=0.031$ for face vs. pupil, $p=0.063$ for locomotion vs. pupil; ΔR^2: $p=0.031$ for face vs. locomotion, $p = 0.063$ for face vs. pupil, $p=0.438$ for locomotion vs. pupil; post-hoc signed rank tests). For both ACh 3.0 and jRCamp1b, FaceMap PCs explained most of the variance in the data, with the first component alone outperforming other behavioral metrics (Figure S6). These results indicate that cholinergic release, like intracortical dynamics[8, 9], encodes some forms of motor behavior and that distinct behavioral states are differentially coupled to neural activity. Statistical results for these and all subsequent analyses are listed in Supplemental Tables 2 and 3.

State-dependent variation in brain activity might be accompanied by either transient or sustained changes in cholinergic and calcium signals that reflect underlying circuit dynamics. Therefore, we focused on discrete epochs of motor activity and identified timepoints corresponding to the onset of either locomotion or facial movements (Figure 3a, see Methods). Facial movement onset (quantified using FaceMap PC1) in the absence of locomotion was associated with desynchronization of local neuronal firing as estimated by ECoG and significant whole cortex-averaged transients in both ACh (0.64±0.09 $\Delta F/F$,

p=0.001, Student's t-test, n= [46]6 mice) and calcium (0.69±0.15 ΔF/F, p=0.006, Student's t-test, n = 6 mice) signals (Figure S7). Locomotion onset co-occurred with an increase in facial movement and local desynchronization and was also associated with transient increases in ACh (0.68±0.17 ΔF/F, p=0.010, Student's t-test, n=6 mice) and calcium (1.50±0.11 ΔF/F, p<0.001, Student's t-test, n=6 mice) signals (Figure S7). ACh transients varied significantly across cortical areas (p<0.001) but were not significantly different between locomotion and facial motion onsets (p=0.734, two-way repeated measures ANOVA, n=6 mice per group). Calcium transients varied significantly across cortical areas (p<0.001) and states (p=0.005, two-way repeated measures ANOVA, n=6 mice per group), with locomotion onset associated with the largest signal (Figure S7). We also found a significant anterior-posterior gradient in the transient magnitudes for cholinergic but not calcium signals (Figure S7).

Next, we analyzed periods of sustained low or high motor activity (Figure 3a, see Methods). We observed that quiescence included epochs of both low and high facial movement, whereas locomotion always co-occurred with high facial movement, suggesting that arousal might follow a progression from absence of motor activity, to facial motion, to locomotion. Sustained increases in facial movement and locomotion were associated with progressively increasing local circuit desynchronization, as evidenced by an increase in high frequency power (main effect of state on 30–100 Hz: $p < 0.001$, repeated measures ANOVA; High vs. Low facial motion: p=0.048, Locomotion vs. High facial motion: p=0.002, post hoc LSD tests) (Figure 3b) and a corresponding decrease in low frequency power (Figure S7) in the ECoG. We then examined the relationship of these three sustained states with cholinergic and calcium activity across cortical areas. ACh activity varied significantly across cortical areas (p<0.001) and differed by state (p=0.015, two-way repeated measures ANOVA, n=6 mice per group). Sustained facial motion significantly elevated whole-cortex Ach activity (Low facial motion: −0.13±0.04 ΔF/F, High facial motion: 0.18±0.08 ΔF/F; Low vs. High: p=0.046, post-hoc Least Significant Difference (LSD) test) but locomotion did not further increase the Ach signal (Locomotion: 0.16±0.06 ΔF/F; Locomotion vs High facial motion: p=0.717, post-hoc LSD test; Figure 3c). Similarly, sustained calcium activity varied significantly for cortical area (p<0.001) and state (p=0.005, two-way repeated measures ANOVA, n=6 mice per group). Sustained facial movement and locomotion both increased whole cortex calcium activity (Low facial motion: −0.02±0.02 ΔF/F, High facial motion: 0.17±0.04 ΔF/F, Locomotion: 0.63±0.19 ΔF/F; Low vs. High facial motion: p=0.020, Locomotion vs High facial motion: p=0.044, post-hoc LSD test) (Figure 3c). As with transients, there was a significant anterior-posterior gradient in the differences across states measured with Spearman's rank correlation for the cholinergic signal comparing sustained high and low facial movement and for calcium activity comparing sustained locomotion and high facial movement (Figure S7). We also confirmed that these results were not unique to imaging ACh release directly, as we observed a similar relationship between behavioral state and cholinergic axonal signaling measured via mesoscopic imaging of genetically targeted GCaMP6s-expressing fibers (Figure S8).

Our results indicate that increased motor activity (e.g., facial movement) is associated with significantly higher ACh release in motor versus visual areas (Figure 3d). To experimentally

test whether this spatial heterogeneity corresponds to differential modulation of neural circuits, we examined the consequences of pharmacologically manipulating cholinergic receptors (see Methods). Consistent with ACh3.0 imaging, treatment with the muscarinic blocker scopolamine selectively decreased cortical activity in motor but not visual areas (Figure 3e, Supplemental Table 2). In contrast, treatment with the nicotinic blocker mecamylamine had no significant impact on cortical activity (Figure 3e). Together, these results suggest a spatially heterogeneous and state-dependent relationship between cortical ACh release and cortical activity.

State-dependent modulation of cortical network architecture

Behavior is thought to rely on large-scale coordination of activity between cortical areas[50–52]. Therefore, we next examined the spatiotemporal relationships of both ACh and calcium signals by measuring pairwise correlations between cortical regions. We focused on sustained periods of low facial movement, high facial movement, and locomotion, allowing us to test whether these behavioral states with different average increases in fluorescence signals also correspond to distinct changes in network organization. We found that increased facial movement was associated with significant increases in between-area pairwise correlations in anterior somatosensory and motor areas for ACh signal and broad, significant increases for calcium signal (Figure 4a,b, S9, adjusted $p<0.01$, Benjamini-Yekutieli FDR corrected permutation test for each pair, n=6 mice). In marked contrast, locomotion was associated with a reduction in the between-area correlations of cholinergic activity that was significant across the cortex (Figure 4a, adjusted $p<0.01$, Benjamini-Yekutieli FDR corrected permutation test for each pair, n=6 mice). Locomotion also occurred with modest decreases in correlation for calcium signals that were significant primarily across posterior cortical areas (Figure 4b). We note that the limited number of pixels present for the most lateral CCFv3 parcels likely decreases the robustness of correlation measurements for these areas. Overall, our results suggest that moderate levels of arousal (i.e., facial movement without locomotion) generally enhance the coordination of ACh release in the cortex, but further increases in arousal (i.e., locomotion) profoundly decorrelate cholinergic signals, emphasizing the spatiotemporal independence of cholinergic modulation. Moreover, in contrast to the local network decorrelation associated with enhanced arousal (observed in the ECoG data), we find that facial movement is linked to significantly increased correlation across large-scale networks as measured by calcium imaging.

Increases in cholinergic signaling have been linked to enhanced local neuronal firing and response gain[6, 19, 25, 53, 54]. We therefore investigated whether ACh and calcium signals are coupled to each other within individual cortical areas and whether this relationship varies with behavioral state. Sustained facial movement was associated with a significant increase in correlation between the two signals broadly across the cortex (Figure 5a-b, S9, adjusted $p<0.01$, Benjamini-Yekutieli FDR corrected permutation test for each pair, n=6 mice). In striking contrast, sustained locomotion was associated with a significant reduction in the correlation between the two channels that was restricted to the frontal cortex (Figure 5a-b, S9, adjusted $p<0.01$, Benjamini-Yekutieli FDR corrected permutation test for each pair, n=6 mice). These data suggest that cholinergic coupling to neuronal activity varies with both cortical area and behavioral state. Overall, our findings demonstrate a spatially

compartmentalized relationship between cholinergic modulation and cortical activity that is diversely dependent on transitions between distinct behavioral states.

Discussion

Despite a long history of investigation into the role of cholinergic modulation in the neocortex, experimental challenges to large-scale simultaneous monitoring of ACh release and neural activity *in vivo* have limited our understanding. Indeed, consistent observations that ACh is coupled to salient behavioral cues across sensory modalities might suggest this modulatory pathway serves as a global, homogeneous influence throughout the cortex[13, 55]. Here, we challenged this view using a combination of mesoscopic imaging and newly developed reporters of both calcium and ACh in behaving mice. Our results clearly demonstrate that cholinergic signaling exhibits substantial spatiotemporal fluctuations that are differentially related to distinct behavioral states, defined by patterns of motor activity.

Both facial movements and locomotion are associated with significant, broad increases in ACh release that are enhanced for anterior versus posterior areas. This anterior-posterior gradient could map onto slightly differential cholinergic projection densities in the frontal versus parietal and occipital areas, to rough anteroposterior and medio-lateral projection topography from the basal forebrain, and/or to different ratios of basal forebrain cholinergic to non-cholinergic (GABAergic) projections for frontal and posterior cortical areas[32, 56, 57]. Interestingly, we find that facial movement is coupled to significantly synchronized ACh release across the anterior cortex. In contrast, locomotion, which co-occurs with facial movement, is coupled to robust, cortex-wide desynchronization of cholinergic activity. This result emphasizes the fundamental independence of cholinergic signaling across different cortical areas and is consistent with anatomical and electrophysiological heterogeneity within populations of cholinergic projection neurons in the basal forebrain[32, 34, 35, 58, 59]. We speculate that information about behavioral states is relayed broadly to the entire basal forebrain, which then propagates independently via discrete channels to selective areas of the cortex. Such a system would allow independent, behavior-specific modulation of cortical subnetworks. We also note that ACh can be released locally by subpopulations of cortical interneurons, providing an additional mechanism for heterogeneous cholinergic modulation[60].

Motor behavior is closely linked to fluctuations in the activity of neurons across the neocortex, suggesting that the representation of movement is a fundamental feature of cortical networks[8, 9, 61]. Here, we find similarly that facial movements and locomotion are represented in ACh signals. Regression analyses suggest that facial motor information is most prominent, contrasting with recent observations showing that cholinergic axonal activity is strongly coupled to pupil dynamics[47]. We note that, unlike axonal calcium imaging, ACh3.0 reports cholinergic release and the transfer function between presynaptic calcium and transmitter exocytosis *in vivo* is poorly characterized[62]. In this way, our approach is similar to electrochemical measurement of cholinergic release[63] but capable of stable, longitudinal monitoring across the entire dorsal cortex in the absence of invasive probes. Nevertheless, we found similar spatial patterns of cholinergic signaling while imaging either ACh release (via ACh3.0) or presynaptic axonal activity (via GCaMP6s),

suggesting our results are not specific to signal modality. Importantly, none of these methods provide information regarding the physiological extent of ACh reception or cell type-specific downstream signaling, which ultimately requires tools for monitoring both postsynaptic biochemical activity and spike output at cellular resolution[64].

In the neocortex, both motor activity and cholinergic signaling have been linked to the desynchronization of local circuits and the decorrelation of spiking between neighboring neurons[6, 22, 23, 25, 65]. Such electrophysiological changes are suggested to enhance the representation of information, particularly under demanding cognitive regimes such as focused attention[66]. However, the coordination of sensory, motor, and cognitive networks is also thought to be necessary for behavior[1, 8, 9, 67]. Here, we find the surprising result that increasing motor activity and ACh release are associated with significant increases in long-range, intracortical correlations even though local circuits are decorrelated.

The appreciation for behavioral state as a critical determinant of cortical function and behavior has only increased in recent years, although the diversity of studies has left a number of ambiguities unresolved. For example, variations in arousal, attention, locomotion, whisking, facial movements, and pupil diameter have all been linked to cortical dynamics and modulation of perceptual ability [1–4, 9, 45]. The extent to which these categorizations reflect distinct or overlapping mechanisms and computations remains largely unknown. Indeed, previous work found that arousal without locomotion and arousal accompanied by locomotion exert distinct influences on local cortical activity patterns, but both enhance sensory encoding[3]. Nevertheless, our findings here underscore the hypothesis that waking comprises diverse behavioral states characterized by specific patterns of neuromodulatory dynamics[3, 13]. Indeed, our data suggest that arousal and neuromodulation may follow a progression that parallels motor activity, first manifesting with facial movement and increasing with locomotion (Figure 6). In this model, moderate arousal drives increased ACh release and cortical activity that is coupled to a decorrelation of local circuits and enhanced large-scale synchrony. Further arousal associated with locomotion drives desynchronized ACh release, local circuit decorrelation, and global correlation of broad intracortical networks. The causal links between these dynamics remain to be determined. However, the advent of multi-color fluorescent reporters, novel combinations of imaging modalities and electrophysiology[11, 12, 38, 68], and further refinement of behavioral analyses[9, 69] will open further avenues into resolving these issues.

In conclusion, we provide novel evidence for the idea that movement is broadly represented in the cortex, not only in local circuit activity[8, 9] but also in the dynamics of cholinergic modulation. Furthermore, cholinergic output during movement is spatially structured and non-uniform in the cortex. Additional studies are required to determine whether these common patterns reflect movement-related ascending regulation of cortical networks or top-down, state-dependent control of basal forebrain output[13]. In either case, we propose the broad hypothesis that the fine-tuned orchestration of behavioral and cortical state dynamics requires coordinated coupling of neuronal activity and cholinergic modulation within distinct, spatially heterogeneous networks of the neocortex.

Materials and Methods:

Animals

Male and female C57BL/6J, ChAT-Cre (B6J.ChAT-IRES-Cre::frt-neo-frt, Jax stock no. 028861), Slc17a7-cre/Camk2α-tTA/TITL-GCaMP6f (JAX stock no. 023527, 024108), and Thy1-GCamp6f (JAX stock no. 024276) mice were kept on a 12h light/dark cycle, provided with food and water ad libitum, and housed individually following headpost implants. Imaging experiments were performed during the light phase of the cycle. All animal handling and experiments were performed according to the ethical guidelines of the Institutional Animal Care and Use Committee of the Yale University School of Medicine.

Neonatal sinus injections

Brain-wide expression of the ACh sensor ACh3.0 and the calcium indicator jRCaMP1b was achieved via postnatal sinus injection[11, 39]. Specifically, P0-P1 litters were removed from their home cage and placed on a heating pad. Pups were kept on ice for 5 min to induce anesthesia via hypothermia and then maintained on a metal plate surrounded by ice for the duration of the injection. Under a dissecting microscope, two small incisions were made in the skin over the transverse sinuses. Viral injections were made with a NanoFil (WPI) attached to a 36-gauge needle and an UltraMicroPump (WPI) mounted to a stereotaxic arm. The needle was slowly lowered through the skull into the underlying transverse sinus. Pups were injected bilaterally with 2 μl of AAV9-hsyn-ACh3.0 (1.8×10^13 gc/ml) and 2 μl of AAV9-hsyn-NES-jRCaMP1b (2.5×10^13 gc/ml, Addgene) per hemisphere. The hsyn promoter drives expression in most excitatory neurons. Subset of pups were bilaterally injected with 4 μl AAV9-hsyn-EGFP (3.4×10^13 gc/ml, Addgene) or 4 μl AAV9-hsyn-ACh3.0 (1.8X10^13 gc/ml) per hemisphere or a combination of 2 ul AAV9-hsyn-EGFP (3.4X10^13, Addgene) and AAV9-hsyn-mCherry (3.6X10^13, Addgene) per hemisphere. Viruses were injected at 10 nl/s, and the needle was left in the sinus for 30 s following the injection. Incision sites were sealed with Vetbond glue, and pups were moved to a heating pad. Once the entire litter was injected, pups were gently rubbed with home cage bedding and nesting material and returned to their home cage. Chat-Cre$^{+/0}$Ai162$^{F/0}$ [70] mice endogenously expressed GCamp6s in cholinergic neurons and terminals and were not injected with virus. Similarly, Slc17a7-cre/Camk2α-tTA/TITL-GCaMP6f and Thy1-GCaMP6f mice expressed GCaMP6f in cortical excitatory neurons.

Surgical procedures

All surgical implant procedures were performed on adult mice (>P50). Mice were anesthetized using 1-2% isoflurane and maintained at 37°C for the duration of the surgery. The skin and fascia above the skull were removed from the nasal bone to the posterior of the intraparietal bone and laterally between the temporal muscles. The surface of the skull was thoroughly cleaned with saline and the edges of the incision secured to the skull with Vetbond. A custom titanium headpost was secured to the posterior of the nasal bone with transparent dental cement (Metabond, Parkell), and a thin layer of dental cement was applied to the entire dorsal surface of the skull. Next, a layer of cyanoacrylate (Maxi-Cure, Bob Smith Industries) was used to cover the skull and left to cure ~30 min at room temperature to provide a smooth surface for transcranial imaging.

For simultaneous ECoG implants, a dental drill was used to make a small craniotomy (~1mm) lateral to V1 in the right hemisphere. A silver ball electrode was placed in the craniotomy and a teflon coated silver reference wire implanted in the contralateral cerebellar hemisphere. A ground wire was wrapped around a skull screw placed in the ipsilateral intraparietal bone. For simultaneous basal forebrain stimulation in a subset of animals, stainless steel bipolar stimulating electrodes (125 um diameter, Invivo1) were implanted at the following coordinates (AP = −0.5 mm, ML = 1.6 mm, DV = 4 mm, angle = 0 degrees or AP = −0.5 mm, ML = 3.3 mm, DV = 3.7 mm, angle = 20 degrees) to target the nucleus basalis in the right hemisphere. Stimulation comprised a brief burst at 100 Hz (1 ms pulse width, 20 pulses, 60–100 uA). Desynchronization in cortical ECoG was used to verify correct electrode placement and to titrate the stimulation intensity.

Widefield imaging

Widefield calcium and cholinergic imaging was performed using a Zeiss Axiozoom with a PlanNeoFluar Z 1x, 0.25 numerical aperture objective with a 56 mm working distance. Epifluorescent excitation was provided by an LED bank (Spectra X Light Engine, Lumencor) using three output wavelengths: 395/25, 470/24, and 575/25 nm. Emitted light passed through a dual camera image splitter (TwinCam, Cairn Research) then through either a 525/50 or 630/75 emission filter (Chroma) before it reached two sCMOS cameras (Orca-Flash V3, Hamamatsu). Images were acquired at 512×512 resolution after 4x pixel binning, and each channel was acquired at 10 Hz with 20 ms exposure. Images were saved to a solid-state drive using HCImage software (Hamamatsu).

Backscatter illumination was provided by LEDs (Thorlabs M530L4, M625L4) centered and narrowly filtered at 530 nm and 625 nm coupled to a 1000 um diameter bifurcated fiber (BFY1000LS02) that terminated 45 degrees incident to the brain surface. Image frames capturing backscatter at 530 and 625 nm were acquired at 10 Hz and interleaved with the usual fluorescence emission acquisition.

All imaging was performed during the second half of the light cycle in awake, behaving mice that were head-fixed so that they could freely run on a cylindrical wheel[3, 4, 71]. A magnetic angle sensor (Digikey) attached to the wheel continuously monitored wheel motion. Mice received at least three wheel-training habituation sessions before imaging to ensure consistent running bouts (see Figure S4). During widefield imaging sessions, the face (including the pupil and whiskers) was illuminated with an IR LED bank and imaged with a miniature CMOS camera (Blackfly s-USB3, Flir) with a frame rate of 10 Hz. To monitor the ECoG, we used a DP-311A differential amplifier with active headstage (Warner Instruments). Signals were amplified 1000x, filtered between 0.1Hz and 1000 Hz, and digitized at 5000 Hz using a Power 1401 acquisition board (CED).

Visual stimulation and air-puffs

Small (20 degree diameter) sinusoidal drifting gratings (2 Hz, 0.04 cycles/degree, 100% contrast) were generated using Psychtoolbox in MATLAB and presented on an LCD monitor at a distance of 20 cm. Stimuli were presented for 1–2 seconds.. Air-puff stimuli

were delivered using a thin metal tube aimed at the fur along the back and coupled to a solenoid valve (Clark Solutions) that delivered brief (200 ms) puffs of compressed air.

Histology

Histological validation was performed on a subset of animals at the conclusion of imaging experiments. Mice were deeply anesthetized with isoflurane and perfused transcardially with phosphate buffered saline (PBS) followed by 4 percent paraformaldehyde in PBS. Brains were postfixed overnight at 4 degrees and embedded in 1% agarose, and 50 um sagittal sections were cut on a vibratome (VT1000, Leica). Slices were pretreated in blocking solution (2 percent normal goat serum, 0.1 percent Triton X-100 in PBS) for four hours then incubated with primary antibodies at 1:1000 (either rabbit anti-GFP and guinea pig anti-NeuN, Invitrogen, or mouse anti-GFP and rabbit anti-GABA, Invitrogen) at 4 degrees for 24 hours. The following day, slices were washed with PBS and incubated in secondary antibodies (either anti-rabbit-Alexa Fluor 488 and anti-guinea pig-Alexa Fluor 647, Invitrogen, or anti-mouse-Alexa Fluor 488 and anti-rabbit 647, Invitrogen) at 1:1000 for two hours at room temperature. Slices were washed 3 times in PBS then mounted on glass slides in Vectashield antifade mounting medium (Vector Laboratories). Widefield images were acquired on an Olympus BX53 fluorescence microscope. Confocal images were taken with a Zeiss LSM 900.

ACh3.0 imaging *ex vivo*

Under isoflurane anesthesia, mice were decapitated and coronal slices (~300 um thick) were cut in ice-cold external solution containing (in mM): 100 choline chloride, 25 NaHCO3, 1.25 NaH2PO4, 2.5 KCl, 7 MgCl2, 0.5 CaCl2, 15 glucose, 11.6 sodium ascorbate and 3.1 sodium pyruvate, bubbled with 95% O2 and 5% CO2. Slices were transferred to artificial cerebrospinal fluid (ACSF) containing (in mM): 127 NaCl, 25 NaHCO3, 1.25 NaH2PO4, 2.5 KCl, 1 MgCl2, 2 CaCl2 and 15 glucose, bubbled with 95% O2 and 5% CO2. After an incubation period, slices were moved to a modified recording chamber under the objective of the widefield microscope and constantly perfused with oxygenated ACSF. Slices were imaged using the same protocol as during *in vivo* imaging sessions (10 Hz, 20 ms exposure). A glass pipette filled with 20 millimolar carbachol was mounted in a micromanipulator and lowered to just above the slice. A Picospritzer (Parker Hannifin Corp) was used to deliver 200 ms puffs of carbachol. During some trials, scopolamine (20 uM) was added to the ACSF before carbachol puffs were applied.

Pharmacology—Animals were injected with either saline, scopolamine hydrobromide (Tocris Bioscience, 0.5 mg/kg, i.p.), or mecamylamine hydrocholoride (Tocris Bioscience,1mg/kg, i.p.) 15 min before imaging sessions. The order of drug/vehicle injection across sessions was randomized across animals.

Data analysis

All analyses were conducted using custom-written scripts in MATLAB (Mathworks) and Prism9 (GraphPad). All statistical results are listed in Supplemental Table 2. Exact correlation values and p-values for Figures 4 and 5 are shown in Supplemental Table 3.

Histology Analysis—For cellular quantification, two fields of view in each region were captured per mouse using a 10x objective (Zeiss). jRCaMP1b-positive cells were identified using the Analyze Particles function in ImageJ. Expression of either ACh3.0 or GABA was assessed by first quantifying the density of signal for each cell and comparing to a null distribution from a pixel-shifted control image. Expression was considered positive for cells with signal greater than two standard deviations above control. Statistical comparisons between frontal, somatosensory, and visual areas were made using a one way repeated measures ANOVA.

Preprocessing of imaging data—512×512 images were down-sampled to 256×256, and frames were grouped by excitation wavelength (395 nm, 470 nm, 575 nm). For dual color imaging, green and red images were acquired using different cameras and registered via automatic 'rigid' transformation using imregtform in MATLAB. In some cases, registration points were manually selected and a 'similarity' geometric transformation was applied. Images were then detrended and baseline corrected to calculate ΔF/F images. Specifically, for each pixel, a 100th order fir1 filter with 0.001 Hz frequency cutoff was applied to extract the low pass filtered signal. This low pass signal was used as baseline (F0), and ΔF/F for each pixel was calculated as (F−F0)/F0, where F is the raw unfiltered signal. ΔF/F values were used for all subsequent analyses. Images were registered to the Allen Common Coordinate framework (CCFv3) using manually selected control points and 'similarity' based geometric transformation. Time series for individual brain parcels were then extracted by averaging ΔF/F values across all pixels within a parcel.

Hemodynamic correction—Common methods for correction of hemodynamic artifacts are typically based on linear regression of a neural activity-dependent signal against an activity-independent signal and performed on a pixel-by-pixel basis, ignoring the spatial correlations among neighboring pixels that exist within and between the two signals. However, accounting for such correlations can be advantageous for mitigating the effects of noise. We experimentally confirmed that excitation of ACh3.0 with 395 nm light results in fluorescence with substantially reduced dependence on ACh (Figure S2), enabling us to use this approach to correct the signal collected with 470 nm excitation. We now present our mathematical formulation for hemodynamic artifact removal as the optimal linear predictor for the neuronal time series, given the 470 nm- and 395 nm- excitation signals.

Let y_1 and y_2 be $p \times 1$ random signals corresponding to p pixels of the 470 nm and 395 nm signals, respectively. Let x and z be mutually uncorrelated $p \times 1$ random signals corresponding to p pixels of the ACh-dependent and -independent (hemodynamic) signals, respectively. We consider the following linear model:

$$y_1 = x + z + \eta,$$

$$y_2 = Az + \xi,$$

where η and ξ are white Gaussian $p \times 1$ noise signals and A is an unknown $p \times p$ real invertible matrix. Given the above-mentioned model, our goal is to estimate the signal x.

It can be verified that the optimal linear estimator of x in the sense of Minimum Mean Squared Error (MMSE) is given by:

$$\hat{x} = H\begin{pmatrix} y_1 \\ y_2 \end{pmatrix}, \quad H = \Sigma_{xy}\Sigma_y^{-1},$$

Where $y = \begin{pmatrix} y_1 \\ y_2 \end{pmatrix}$ is given by stacking y_1 on top of y_2, $\Sigma_y = \mathbb{E}\left[yy^T\right]$ is the autocorrelation matrix of y, and $\Sigma_{xy} = \mathbb{E}\left[xy^T\right]$ is the cross-correlation matrix between x and y. While Σ_y can be estimated directly from the observations, this is not trivially the case for Σ_{xy} since it depends on the unknown signal x. Nevertheless, we show below that Σ_{xy} can be expressed as:

$$\Sigma_{xy} = \left(\Sigma_{y_1} - \sigma_\eta^2 I - \left(\Sigma_{y_1y_2}(\Sigma_{y_2} - \sigma_\xi^2 I)^{-1}\Sigma_{y_2}^{-1}\Sigma_{y_1y_2}^T\right)^T 0\right),$$

Where σ_η^2 and σ_ξ^2 are the noise variances of η and ξ, respectively, and I is the $p \times p$ identity matrix. Importantly, all quantities in the formula for Σ_{xy} can be estimated directly from the observations of y_1 and y_2. The noise variances σ_η^2 and σ_ξ^2 were evaluated according to the median of the singular values of the corresponding correlation matrices Σ_{y_1} and Σ_{y_2}.

Proof for the formula for Σ_{xy}:

$$\Sigma_{xy} = \left(\Sigma_{xy_1} \ \Sigma_{xy_2}\right)$$

$$\Sigma_{xy_1} = \Sigma_x$$

$$\Sigma_{xy_2} = 0$$

$$\Sigma_{y_1} = \Sigma_x + \Sigma_z + \Sigma_\eta$$

$$\Sigma_{y_2} = \mathrm{A}\Sigma_z A^T + \Sigma_\xi$$

$$\Sigma_{y_1y_2} = \Sigma_z A^T$$

Using these equations, we can extract $\Sigma_z = \left(\Sigma_{y_1y_2}(\Sigma_{y_2} - \Sigma_\xi)^{-1}\Sigma_{y_2}^{-1}\Sigma_{y_1y_2}^T\right)^T$ which leads to:

$$\Sigma_{xy1} = \Sigma_{y1} - \Sigma_{\eta} - \left(\Sigma_{y1y2}(\Sigma_{y2} - \Sigma_{\xi})^{-1}\Sigma_{y2}^{-1}\Sigma_{y1y2}^{T}\right)^{T}$$

Note that in the case of a single pixel, i.e. $p = 1$, our estimator reduces to a simple regression based on pixelwise correlations. However, taking p to be all pixels at once is both computationally expensive and unnecessary. Therefore, we performed these evaluations locally, where the time trace of each pixel was computed based on a patch of its nearest spatial neighbors. The size of the patch was determined according to the amount of time samples available. Using a bigger patch would lead to bigger covariance matrices to be estimated and therefore requires longer time traces. For our sessions a patch size of 9 × 9 was empirically selected as most adequate.

Validation of hemodynamics correction—The novel spatial regression approach used here was validated by comparing results with other known hemodynamics correction strategies. Several benchmarks were used to determine the effectiveness of our method. First, we and others have observed that strong stimuli, such as a high-contrast visual stimulus, evoke negative dips in fluorescence signals that are driven by hemodynamic photon absorption [41, 42]. Here, we compared this visual stimulus-evoked negativity in V1 of GFP-mCherry expressing mice for uncorrected ΔF/F signals (measured for 470 nm or 575 nm excitation) and ΔF/F signals corrected by either spatial or pixel-wise regression of signals collected at 395 nm excitation. Visual trials were normalized by subtracting the baseline mean in the −2 to 0 s pre-stimulus period, and the minimum normalized ΔF/F values at 0 to 5 s after stimulus onset were calculated for each trial. These values were then averaged across all trials in an animal, and statistical comparisons were made within mice between the three methods using protected paired t-tests following repeated measures ANOVA. A complementary approach involves the measurement of hemodynamic absorption from changes in the reflectance (“backscatter”) of green photons while simultaneously performing fluorescence imaging [41, 42]. Here, we carried out pixel-wise and spatial regression of uncorrected ΔF/F signals using 530 nm backscatter data and compared results with 395 nm-based correction. We also determined the spatial homogeneity of hemodynamic correction with the different correction methods by examining the averaged visual stimulus-evoked negativity in GFP and mCherry fluorescence across all cortical parcels. Furthermore, we compared the visual stimulus-evoked negativity of Ach 3.0 in V1 for uncorrected ΔF/F signals (measured for 470 nm excitation) and ΔF/F signals corrected by either spatial or pixel-wise regression of signals collected at 395 nm excitation. Finally, we also assessed the efficiency of the different correction approaches to reduce the variance in ΔF/F signals collected from GFP-expressing control mice, where all fluctuations are assumed to result primarily from hemodynamic variation. Statistical comparisons on ΔF/F maximum negativity values post-air-puff were performed in a similar manner as descried above for visual stimuli.

Preprocessing of behavior data—Facial movements were extracted from face videography using FaceMap[9]. The toolbox applies singular value decomposition (SVD) to the face movie to extract the 1000 dimensions or principal components (PCs) that explain

the distinct movements apparent on the mouse's face. Here, we included the top 25 PCs for regression analyses and the first PC for other analyses. To extract face movement states, we focused on quiescence periods only, because locomotion is consistently associated with increased facial motion. First, PC1 data were Z-score normalized within a session, and the high/low thresholds corresponding to 60% and 40% quantiles in the data distribution during quiescence only were extracted for that session. Data were then smoothed using a 1s-window moving average filter, and epochs during which smoothed data continuously exceeded the high/low Z-threshold for at least 0.5 s were considered high/low face state, respectively.

Wheel position was determined from the output of the linear angle detector. The circular wheel position variable was first transformed to the $[-\pi, \pi]$ interval. The phases were then circularly unwrapped to get running distance as a linear variable, and locomotion speed was computed as a differential of distance (cm/s). A change-point detection algorithm detected locomotion onset/offset times based on changes in standard deviation of speed. First, moving standard deviations of speed were computed in 2 s windows, which was the temporal resolution of the changepoint analysis. Initial locomotion onset/offset times were then estimated from periods when the moving standard deviations exceeded/ fell below an empirical threshold of 0.005. These estimates were refined by computing the time points corresponding to the maximum of the moving forward/backward Z-score in 2 s windows around each onset/offset time. Locomotion epochs that were too short (<1s) or where average speed was too low (<2 cm/s) were removed.

Post-processing analysis

Imaging data from individual parcels were used for subsequent analyses. Some medial Allen parcels (PL, ACA, RSPv) were masked out because of prominent vasculature along the midline. Colliculus regions (SC, IC) were also removed, resulting in final 23 Allen CCFv3 parcels per hemisphere (see Figure S2). The primary visual cortex (V1 or VlSp) and the secondary motor area in the frontal cortex (M2 or Mos) were selected as representative areas for some population summaries and statistical comparisons. The anterior-posterior spatial ranking of Allen CCFv3 areas was determined by calculating the relative centers of mass for each parcel (see Figure S2). The ordering was as follows (from anterior to posterior): Mos, Mop, SSp-m, SSp-ul, SSp-n, SSp-ll, SSp-un, SSp-tr, SSp-bfd, SSs, PTLp, VlSam, AUD, RSPagl, RSPd, VlSal, VlSpm, Tea, VlSli, VlSl, VlSp, VlSpor, VlSpl.

Basal Forebrain Stimulation-Evoked Activity—Trials where basal forebrain stimulation caused locomotion were automatically excluded. Data were normalized by subtracting the baseline mean in the pre-stimulus period −2 to 0 s. Difference $\Delta F/F$ data were averaged across all trials within an animal and summarized as mean +/− standard error of mean across animals.

Regression with behavioral variables—Linear regression of continuous data from full imaging sessions was used to predict ACh3.0 and jRCaMP1b activity in each parcel using zero-lagged analog behavioral variables as predictors. 10 fold cross validation was performed by partitioning the time series into 10 chunks and using independent test

partitions in each fold. The prediction accuracy was calculated on testing data in each of the 10 folds and averaged to get a final cross-validated R^2. The full regression model was built using 1–25 FaceMap PCs, pupil area, and wheel speed. The model was fit using ridge regression (ridgeMML.m, Musall et al., 2019) in which the regularization penalty was estimated separately for each parcel using marginal maximum likelihood estimation[8]. Reduced models were generated by shuffling specified variables in time. Cross-validated R^2 values from the reduced models were subtracted from those from the full model to get ΔR^2 values representing the unique contribution of that variable. In addition, single variable models were fit to extract individual cross-validated R^2 values for specified behavioral variables. Friedman's ANOVA was used to assess whether full model cross validated R^2 values are significantly different across brain areas. Spearman's rank-order correlation was used to assess the relationship between mean cross validated R^2 values and Allen-defined parcels' anterior-posterior positioning. Cross-validated R^2 and ΔR^2 values were averaged across parcels in one hemisphere, and comparisons between behavioral variables were performed using a Friedman's ANOVA, followed by post-hoc Wilcoxon signed rank tests.

State Transitions and Sustained States—Behavioral states were categorized into high/low states (high/low face or locomotion/quiescence) based on movement as described above (see preprocessing of Behavior Data). Changes at transition from low to high movement state (face onset or locomotion onset) were defined as state transients (see Figure 3a). For locomotion onset, only locomotion trials that contained at least 5 s of running and were preceded by a minimum 10 s of quiescence were included. For high face state onset, if a high face state was preceded by at least 4 s of a low face state, the transition between the two states was used as the high state onset time point. For each animal, state transients were quantified by first subtracting mean pre-onset (−5 to −3s for locomotion and −4 to −2s for face) from post-onset ΔF/F values and averaging data across all state transitions, then calculating the peak ΔF/F value at 0 to 1 s after onset. Whole cortex-averaged transients were obtained by averaging peak ΔF/F values across all parcels in one hemisphere, and a one-sample Student's t-test was conducted to test significant differences from zero. A two-way repeated measures ANOVA was used to assess any significant differences in state transients across brain areas and behavioral states. Spearman's rank-order correlation was used to assess the relationship between mean peak ΔF/F values and Allen-defined parcels' anterior-posterior positioning.

Sustained behavioral states were defined as high or low movement states that persisted for several seconds (see Figure 3a). For sustained locomotion states, it was required that locomotion started at least 3 s before and ended at least 3 s after the state boundaries. Similarly, for sustained quiescence states, it was required that any locomotion did not occur at least 10 s before and 10 s after a given period. Sustained high/low face states were extracted during quiescence only. The minimum duration of sustained states was set to 5s. State data were then compared between low FaceMap, high FaceMap, and locomotion states. To ensure accurate comparison between states, the number of state epochs and total duration within each epoch were matched across states within each session. ACh3.0, RCaMP1b, and Chat-Gcamp6s ΔF/F responses during these three states were quantified for

each parcel, and whole cortex-averaged responses were obtained by averaging ΔF/F values across all parcels in one hemisphere. A two-way repeated measures ANOVA was used to assess whether ΔF/F responses varied across brain areas and behavioral states, followed by post-hoc LSD tests to test differences between high and low FaceMap states as well as locomotion and high FaceMap state. The response to facial movement and locomotion were quantified as difference between high and low FaceMap ΔF/F values and between locomotion and high FaceMap ΔF/F values, respectively. Spearman's rank-order correlation was used to assess the relationship between difference ΔF/F values and anterior-posterior rank of Allen-defined parcels. Ach 3.0 amplitude during high FaceMap state was compared between frontal-motor areas (averaged ΔF/F across areas MOp and MOs) and visual areas (averaged ΔF/F across areas VISp, VISpm, VISam, VISI, VISli, VISpl, VISpor, VISal) with a paired t-test.

For the pharmacology experiments, the effect of drug on high face motion related cortical activity in frontal-motor or visual areas was computed by taking a difference of ΔF/F between drug and saline sessions within each animal and performing one-sample t-tests. The spatial difference in drug's effects between visual and motor areas was assessed via paired t-tests on the difference ΔF/F values between visual and motor areas.

ECoG processing—The multitaper spectrogram in Figure 1 was estimated from the raw ECOG signal using the Chronux toolbox (using sliding windows of 3 s with 0.5 s overlap). ECoG power was calculated for each behavioral state by estimating the bandpower in high (30–100 Hz) and low frequency (1–10 Hz) bands. The ECoG high and low frequency power values were compared between high versus low FaceMap and locomotion versus high FaceMap states using Student's paired t-tests.

State-dependent correlations—Time-lagged correlations between every pair of Allen CCF parcels in Ach 3.0 or jRCaMP1b signals were computed by performing cross-correlations with 500 ms time lag and extracting the maximum correlation coefficient. The resulting parcel-wise correlation matrices were calculated during sustained behavioral states with a minimum duration of 5 s to allow enough time frames for lagged correlations. To ensure accurate comparison in correlations between states, the number of state epochs and total duration within each epoch were matched for locomotion, high, and low facial movement states within each session. Correlation matrices were calculated for each state epoch and averaged all epochs and sessions for each animal to get one correlation matrix per animal per state. Cross-correlations between Ach 3.0 and jRCaMP1b activity for distinct behavioral states were calculated in a similar manner except the correlations were performed between the two signals within a parcel. Correlation matrices were compared between locomotion versus high facial motion states as well as high facial motion versus low facial motion states. To assess the significance of differences in pairwise correlations between states (high versus low facial motion and locomotion versus high facial motion), a stratified permutation test was used. In each permutation, state labels were shuffled across epochs within each animal, and the corresponding correlation matrices were averaged across all epochs of a particular state to get one permuted correlation matrix per state per animal. These values were then averaged across animals to get a mean difference between states.

This was repeated 10,000 times to build a null distribution of mean differences which was compared against the observed mean difference to determine p-values. Multiple comparisons correction was performed by setting the false discovery rate (FDR) to $q < 0.01$ and using Benjamini-Yekutieli method in fdr_bh.m toolbox in MATLAB. Correlation values and adjusted p-values are available in the Supplemental Table 3.

Supplementary Material

Refer to Web version on PubMed Central for supplementary material.

Acknowledgements

The authors thank all members of the Higley and Cardin laboratories for helpful input throughout all stages of this study. We thank Rima Pant for generation of AAV vectors. We thank Daniel Barson, Gal Mishne, and Ronald Coifman for helpful discussions regarding the analysis of the data. We thank Quentin Perrenoud for providing the locomotion changepoint analysis code. We thank the GENIE Project for jRCaMP1b plasmids. This work was supported by funding from the NIH (R01MH099045, R21MH121841, and DP1EY033975 to MJH, R01EY022951 to JAC, R01MH113852 to MJH and JAC, EY031133 to AHM, EY026878 to the Yale Vision Core), an award from the Kavli Institute of Neuroscience (to JAC and MJH), a Simons Foundation SFARI Research Grant (to JAC and MJH), a Swebilius Foundation award (to JAC and MJH), a grant from the Aligning Science Across Parkinson's Initiative (to MJH), support from the Ludwig Foundation (to JAC), a BBRF Young Investigator Grant (to SL) and an award from the Swartz Foundation (to HB).

Data Availability Statement

The full datasets generated and analyzed in this study are available from the corresponding authors on reasonable request. All values found in Figures 4 (correlations between pairs of parcels) and 5 (correlations between signals within a parcel) have been made available as an attached excel file.

References

1. McGinley MJ, et al. Waking State: Rapid Variations Modulate Neural and Behavioral Responses. Neuron 87, 1143–1161 (2015). [PubMed: 26402600]
2. Niell CM & Stryker MP Modulation of visual responses by behavioral state in mouse visual cortex. Neuron 65, 472–479 (2010). [PubMed: 20188652]
3. Vinck M, Batista-Brito R, Knoblich U. & Cardin JA Arousal and locomotion make distinct contributions to cortical activity patterns and visual encoding. Neuron 86, 740–754 (2015). [PubMed: 25892300]
4. Tang L. & Higley MJ Layer 5 Circuits in V1 Differentially Control Visuomotor Behavior. Neuron 105, 346–354 e345 (2020). [PubMed: 31757603]
5. Poulet JFA & Crochet S. The Cortical States of Wakefulness. Front Syst Neurosci 12, 64 (2018). [PubMed: 30670952]
6. Chen N, Sugihara H. & Sur M. An acetylcholine-activated microcircuit drives temporal dynamics of cortical activity. Nat Neurosci 18, 892–902 (2015). [PubMed: 25915477]
7. Munoz W. & Rudy B. Spatiotemporal specificity in cholinergic control of neocortical function. Curr Opin Neurobiol 26, 149–160 (2014). [PubMed: 24637201]
8. Musall S, Kaufman MT, Juavinett AL, Gluf S. & Churchland AK Single-trial neural dynamics are dominated by richly varied movements. Nat Neurosci 22, 1677–1686 (2019). [PubMed: 31551604]
9. Stringer C, et al. Spontaneous behaviors drive multidimensional, brainwide activity. Science 364, 255−+ (2019). [PubMed: 31000656]
10. Cardin JA, Crair MC & Higley MJ Mesoscopic Imaging: Shining a Wide Light on Large-Scale Neural Dynamics. Neuron 108, 33–43 (2020). [PubMed: 33058764]

11. Barson D, et al. Simultaneous mesoscopic and two-photon imaging of neuronal activity in cortical circuits. Nat Methods 17, 107–113 (2020). [PubMed: 31686040]
12. Clancy KB, Orsolic I. & Mrsic-Flogel TD Locomotion-dependent remapping of distributed cortical networks. Nat Neurosci 22, 778–786 (2019). [PubMed: 30858604]
13. Lee SH & Dan Y. Neuromodulation of brain states. Neuron 76, 209–222 (2012). [PubMed: 23040816]
14. Buzsaki G, et al. Nucleus Basalis and Thalamic Control of Neocortical Activity in the Freely Moving Rat. Journal of Neuroscience 8, 4007–4026 (1988). [PubMed: 3183710]
15. Chubykin AA, Roach EB, Bear MF & Shuler MG A cholinergic mechanism for reward timing within primary visual cortex. Neuron 77, 723–735 (2013). [PubMed: 23439124]
16. Picciotto MR, Higley MJ & Mineur YS Acetylcholine as a Neuromodulator: Cholinergic Signaling Shapes Nervous System Function and Behavior. Neuron 76, 116–129 (2012). [PubMed: 23040810]
17. Sarter M. & Lustig C. Cholinergic double duty: cue detection and attentional control. Curr Opin Psychol 29, 102–107 (2019). [PubMed: 30711909]
18. Goard M. & Dan Y. Basal forebrain activation enhances cortical coding of natural scenes. Nat Neurosci 12, 1444–1449 (2009). [PubMed: 19801988]
19. Herrero JL, et al. Acetylcholine contributes through muscarinic receptors to attentional modulation in V1. Nature 454, 1110–1114 (2008). [PubMed: 18633352]
20. Constantinople CM & Bruno RM Effects and mechanisms of wakefulness on local cortical networks. Neuron 69, 1061–1068 (2011). [PubMed: 21435553]
21. Eggermann E, Kremer Y, Crochet S. & Petersen CCH Cholinergic signals in mouse barrel cortex during active whisker sensing. Cell reports 9, 1654–1660 (2014). [PubMed: 25482555]
22. Meir I, Katz Y. & Lampl I. Membrane Potential Correlates of Network Decorrelation and Improved SNR by Cholinergic Activation in the Somatosensory Cortex. J Neurosci 38, 10692–10708 (2018). [PubMed: 30373769]
23. Metherate R, Cox CL & Ashe JH Cellular bases of neocortical activation: modulation of neural oscillations by the nucleus basalis and endogenous acetylcholine. J Neurosci 12, 4701–4711 (1992). [PubMed: 1361197]
24. Minces V, Pinto L, Dan Y. & Chiba AA Cholinergic shaping of neural correlations. Proc Natl Acad Sci U S A 114, 5725–5730 (2017). [PubMed: 28507133]
25. Pinto L, et al. Fast modulation of visual perception by basal forebrain cholinergic neurons. Nat Neurosci 16, 1857–1863 (2013). [PubMed: 24162654]
26. Steriade M, Contreras D, Curro Dossi R. & Nunez A. The slow (< 1 Hz) oscillation in reticular thalamic and thalamocortical neurons: scenario of sleep rhythm generation in interacting thalamic and neocortical networks. J Neurosci 13, 3284–3299 (1993). [PubMed: 8340808]
27. Steriade M, Nunez A. & Amzica F. Intracellular analysis of relations between the slow (< 1 Hz) neocortical oscillation and other sleep rhythms of the electroencephalogram. J Neurosci 13, 3266–3283 (1993). [PubMed: 8340807]
28. Gasselin C, Hohl B, Vernet A, Crochet S. & Petersen CCH Cell-type-specific nicotinic input disinhibits mouse barrel cortex during active sensing. Neuron (2021).
29. Hangya B, Ranade SP, Lorenc M. & Kepecs A. Central Cholinergic Neurons Are Rapidly Recruited by Reinforcement Feedback. Cell 162, 1155–1168 (2015). [PubMed: 26317475]
30. Sturgill JF, et al. Basal forebrain-derived acetylcholine encodes valence-free reinforcement. bioRxiv 2020.02.17.953141 (2020).
31. Guo W, Robert B. & Polley DB The Cholinergic Basal Forebrain Links Auditory Stimuli with Delayed Reinforcement to Support Learning. Neuron 103, 1164–1177 e1166 (2019). [PubMed: 31351757]
32. Kim JH, et al. Selectivity of Neuromodulatory Projections from the Basal Forebrain and Locus Ceruleus to Primary Sensory Cortices. J Neurosci 36, 5314–5327 (2016). [PubMed: 27170128]
33. Laszlovszky T, et al. Distinct synchronization, cortical coupling and behavioral function of two basal forebrain cholinergic neuron types. Nat Neurosci 23, 992–1003 (2020). [PubMed: 32572235]

34. Li X, et al. Generation of a whole-brain atlas for the cholinergic system and mesoscopic projectome analysis of basal forebrain cholinergic neurons. Proc Natl Acad Sci U S A 115, 415–420 (2018). [PubMed: 29259118]
35. Zaborszky L, et al. Neurons in the basal forebrain project to the cortex in a complex topographic organization that reflects corticocortical connectivity patterns: an experimental study based on retrograde tracing and 3D reconstruction. Cereb Cortex 25, 118–137 (2015). [PubMed: 23964066]
36. Disney AA & Higley MJ Diverse Spatiotemporal Scales of Cholinergic Signaling in the Neocortex. J Neurosci 40, 720–725 (2020). [PubMed: 31969490]
37. Dana H, et al. Sensitive red protein calcium indicators for imaging neural activity. eLife 5 (2016).
38. Jing M, et al. An optimized acetylcholine sensor for monitoring in vivo cholinergic activity. Nat Methods (2020).
39. Hamodi AS, Martinez Sabino A, Fitzgerald ND, Moschou D. & Crair MC Transverse sinus injections drive robust whole-brain expression of transgenes. Elife 9 (2020).
40. Wang Q, et al. The Allen Mouse Brain Common Coordinate Framework: A 3D Reference Atlas. Cell 181, 936–953 e920 (2020). [PubMed: 32386544]
41. Ma Y, et al. Wide-field optical mapping of neural activity and brain haemodynamics: considerations and novel approaches. Philos Trans R Soc Lond B Biol Sci 371 (2016).
42. Valley MT, et al. Separation of hemodynamic signals from GCaMP fluorescence measured with widefield imaging. J Neurophysiol 123, 356–366 (2020). [PubMed: 31747332]
43. Bennett C, Arroyo S. & Hestrin S. Subthreshold mechanisms underlying state-dependent modulation of visual responses. Neuron 80, 350–357 (2013). [PubMed: 24139040]
44. McGinley MJ, David SV & McCormick DA Cortical Membrane Potential Signature of Optimal States for Sensory Signal Detection. Neuron 87, 179–192 (2015). [PubMed: 26074005]
45. Neske GT, Nestvogel D, Steffan PJ & McCormick DA Distinct Waking States for Strong Evoked Responses in Primary Visual Cortex and Optimal Visual Detection Performance. J Neurosci 39, 10044–10059 (2019). [PubMed: 31672787]
46. Perrenoud Q, et al. Flexible perceptual encoding by discrete gamma events. bioRxiv, 10.1101/2022.1105.1113.491832 (2022).
47. Reimer J, et al. Pupil fluctuations track rapid changes in adrenergic and cholinergic activity in cortex. Nature communications 7, 13289 (2016).
48. Perrenoud Q, et al. Flexible perceptual encoding by discrete gamma events. bioRxiv (2022).
49. Staiger JF & Petersen CCH Neuronal Circuits in Barrel Cortex for Whisker Sensory Perception. Physiol Rev 101, 353–415 (2021). [PubMed: 32816652]
50. Benisty H, et al. Rapid fluctuations in functional connectivity of cortical networks encode spontaneous behavior. bioRxiv, 10.1101/2021.1108.1115.456390 (2021).
51. Rubinov M. & Sporns O. Complex network measures of brain connectivity: uses and interpretations. Neuroimage 52, 1059–1069 (2010). [PubMed: 19819337]
52. Stafford JM, et al. Large-scale topology and the default mode network in the mouse connectome. Proc Natl Acad Sci U S A 111, 18745–18750 (2014). [PubMed: 25512496]
53. Parikh V, Kozak R, Martinez V. & Sarter M. Prefrontal acetylcholine release controls cue detection on multiple timescales. Neuron 56, 141–154 (2007). [PubMed: 17920021]
54. Soma S, Shimegi S, Suematsu N. & Sato H. Cholinergic modulation of response gain in the rat primary visual cortex. Sci Rep 3, 1138 (2013). [PubMed: 23378897]
55. Hasselmo ME & Sarter M. Modes and models of forebrain cholinergic neuromodulation of cognition. Neuropsychopharmacology 36, 52–73 (2011). [PubMed: 20668433]
56. Avendano C, Umbriaco D, Dykes RW & Descarries L. Acetylcholine innervation of sensory and motor neocortical areas in adult cat: a choline acetyltransferase immunohistochemical study. J Chem Neuroanat 11, 113–130 (1996). [PubMed: 8877599]
57. Bigl V, Woolf NJ & Butcher LL Cholinergic projections from the basal forebrain to frontal, parietal, temporal, occipital, and cingulate cortices: a combined fluorescent tracer and acetylcholinesterase analysis. Brain Res Bull 8, 727–749 (1982). [PubMed: 6182962]
58. Chaves-Coira I, Barros-Zulaica N, Rodrigo-Angulo M. & Nunez A. Modulation of Specific Sensory Cortical Areas by Segregated Basal Forebrain Cholinergic Neurons Demonstrated by

Neuronal Tracing and Optogenetic Stimulation in Mice. Front Neural Circuits 10, 28 (2016). [PubMed: 27147975]

59. Gielow MR & Zaborszky L. The Input-Output Relationship of the Cholinergic Basal Forebrain. Cell Rep 18, 1817–1830 (2017). [PubMed: 28199851]
60. Granger AJ, et al. Cortical ChAT(+) neurons co-transmit acetylcholine and GABA in a target- and brain-region-specific manner. Elife 9 (2020).
61. Parker PRL, Brown MA, Smear MC & Niell CM Movement-Related Signals in Sensory Areas: Roles in Natural Behavior. Trends Neurosci 43, 581–595 (2020). [PubMed: 32580899]
62. Sudhof TC Calcium control of neurotransmitter release. Cold Spring Harb Perspect Biol 4, a011353 (2012).
63. Sarter M. & Kim Y. Interpreting chemical neurotransmission in vivo: techniques, time scales, and theories. ACS Chem Neurosci 6, 8–10 (2015). [PubMed: 25514622]
64. Lee SJ, et al. Cell-type-specific asynchronous modulation of PKA by dopamine in learning. Nature (2020).
65. Polack PO, Friedman J. & Golshani P. Cellular mechanisms of brain state-dependent gain modulation in visual cortex. Nat Neurosci 16, 1331–1339 (2013). [PubMed: 23872595]
66. Thiele A. & Bellgrove MA Neuromodulation of Attention. Neuron 97, 769–785 (2018). [PubMed: 29470969]
67. Crochet S, Lee SH & Petersen CCH Neural Circuits for Goal-Directed Sensorimotor Transformations. Trends Neurosci 42, 66–77 (2019). [PubMed: 30201180]
68. Esmaeili V, et al. Divergent sensory processing converges in frontal cortex for a planned motor response. bioRxiv 2020.10.06.326678 (2020).
69. Mathis A, et al. DeepLabCut: markerless pose estimation of user-defined body parts with deep learning. Nature Neuroscience 21, 1281−+ (2018). [PubMed: 30127430]
70. Larsen RS, et al. Activation of neuromodulatory axon projections in primary visual cortex during periods of locomotion and pupil dilation. bioRxiv (2018).
71. Batista-Brito R, et al. Developmental Dysfunction of VIP Interneurons Impairs Cortical Circuits. Neuron 95, 884–895 e889 (2017). [PubMed: 28817803]

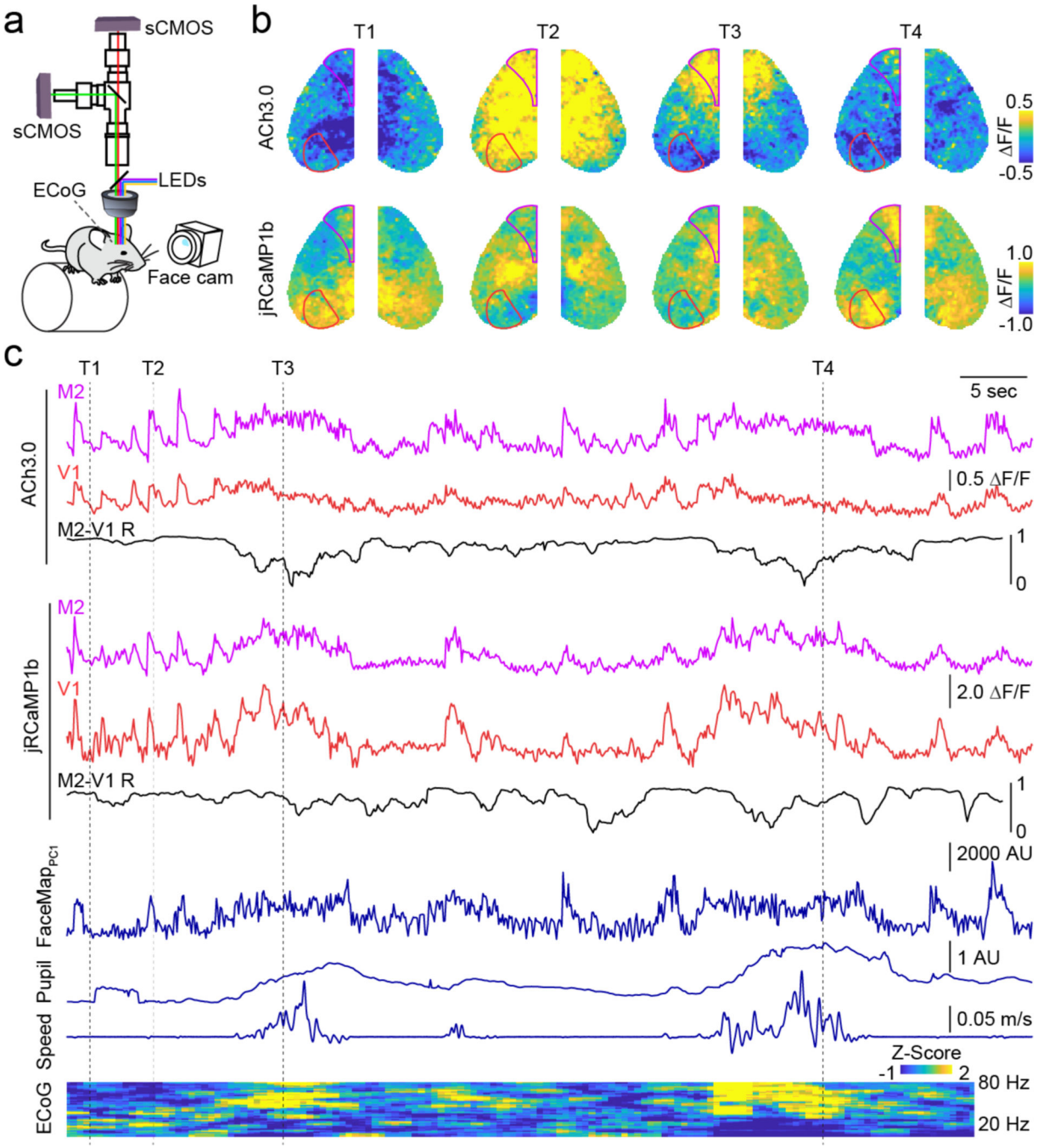

Figure 1. Spatiotemporal dynamics of cholinergic and neural activity in the neocortex.

a, Schematic of the dual wavelength, widefield imaging setup. **b**, Example representative image frames showing fluctuations in cholinergic (ACh3.0, top row) and neural (jRCaMP1b, bottom row) activity across the dorsal cortical surface. Overlaid lines indicate Allen Brain CCFv3-derived parcellation of primary visual cortex (V1) and secondary motor cortex (M2). **c**, Time series for ACh3.0 and jRCaMP1b signals in V1 (red) and M2 (purple) parcels. Instantaneous (3 s window) Pearson's correlation (R) between V1 and M2 is shown beneath

in black. Simultaneous facial motion (FaceMap PC1), pupil area, running speed, and ECoG power spectrogram are shown below. Dashed lines indicate the times of image frames in (b).

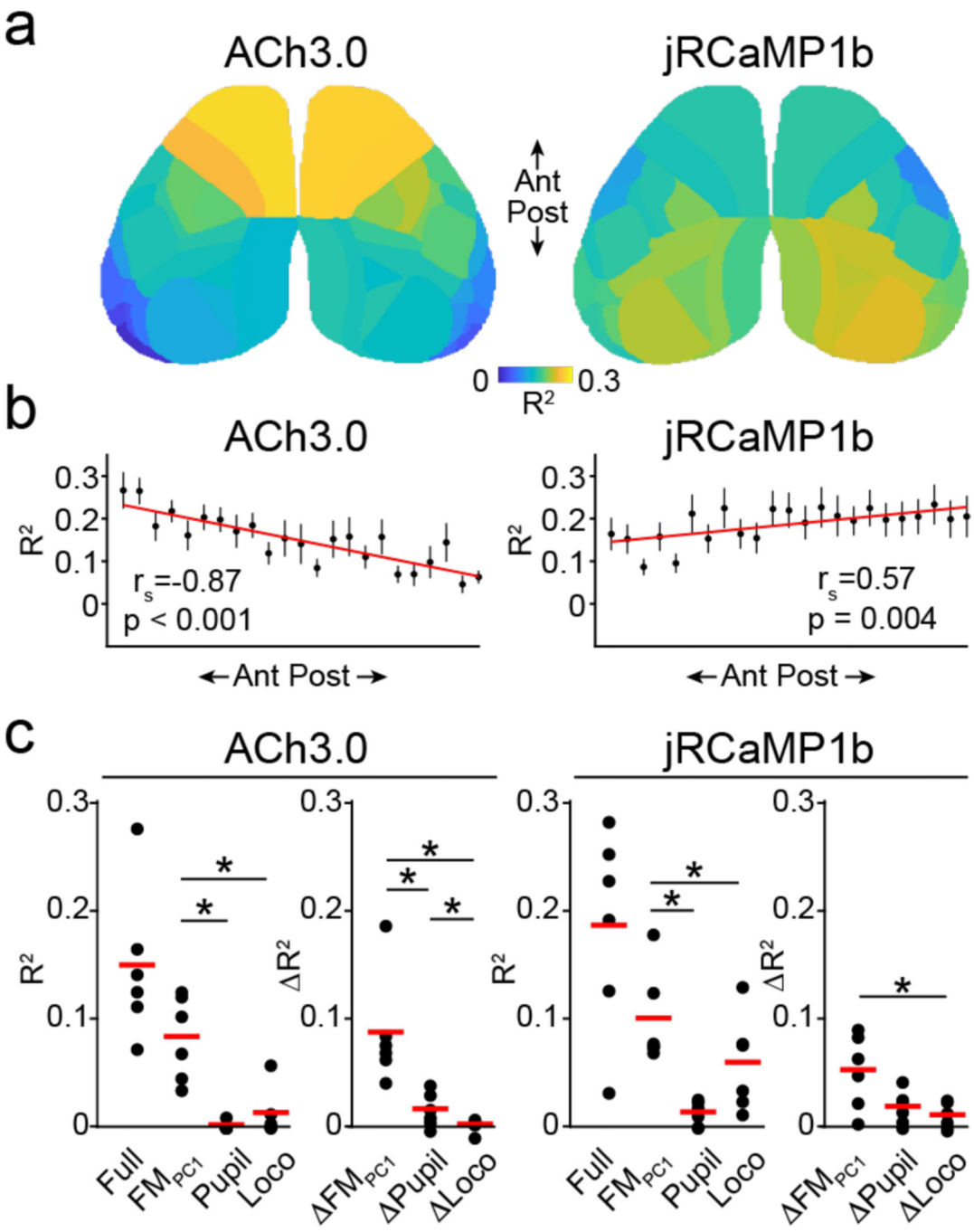

Figure 2. Differential coupling of behavioral variables to cholinergic and neural activity across the neocortex.

a, Average parcel-wise spatial map (n=6 mice) showing ten-fold cross-validated explained variance (R^2) of ACh3.0 (left) and jRcamp1b (right) signals based on a ridge regression model fitted with FaceMap (PC1–25), locomotion, and pupil area. **b**, Allen Brain CCFv3 parcels from one hemisphere were ordered from anterior to posterior based on their center of mass. Cross-validated full model R^2 values (mean ± SEM) of ACh3.0 (left) and jRCaMP1b (right) are plotted against the parcel's anterior to posterior position. r_s indicates Spearman's

rank order correlation coefficient for the correlation between mean R^2 and anterior-posterior rank across parcels. Red line indicates linear fit for visualization purposes. **c**, For each signal, left panels show the cross-validated R^2 for the full model (Full) and for single variable models (FaceMap PC1, pupil area, locomotion). Right panels show the unique contribution of each variable (ΔR^2). *indicates $p < 0.05$ for Wilcoxon signed rank tests following a significant Friedman's ANOVA.

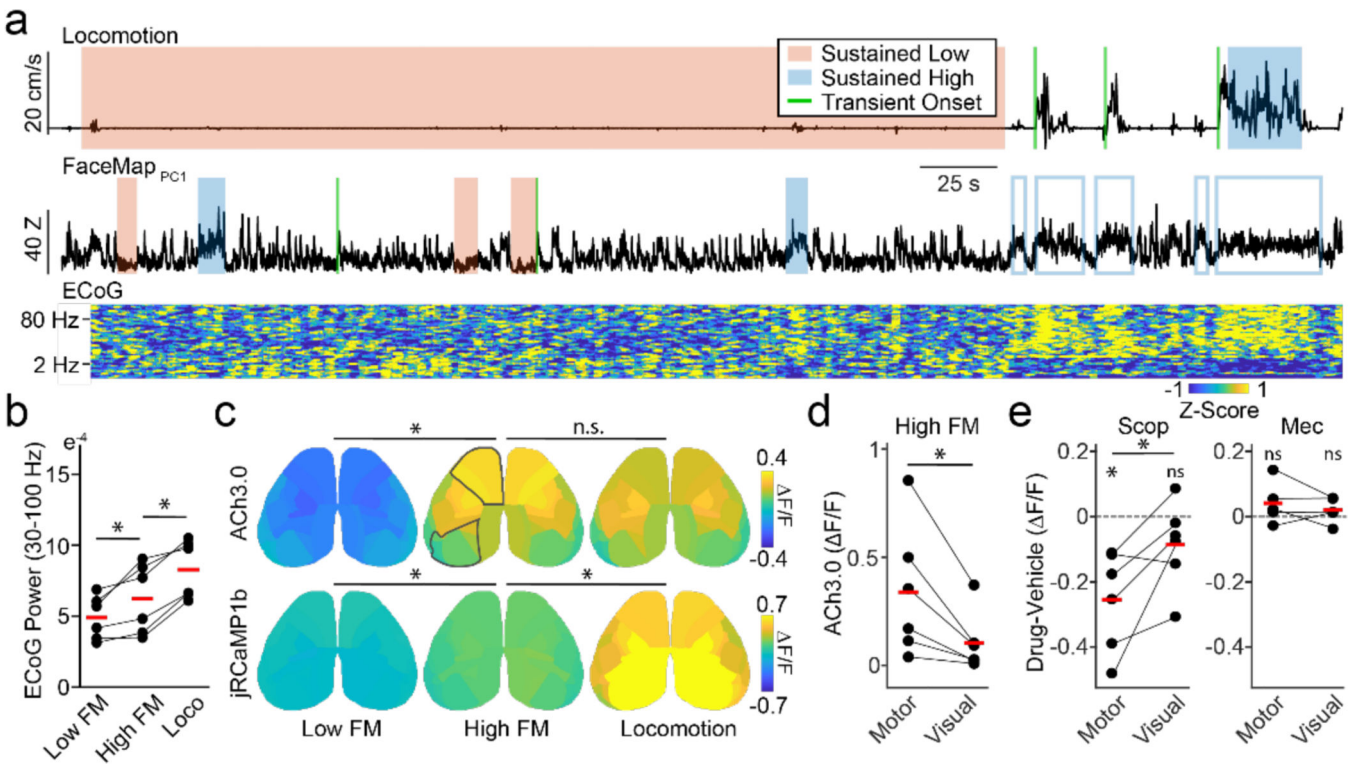

Figure 3. Cholinergic and neural signal heterogeneity during movement-defined behavioral states.

a, Example locomotion (top) and FaceMap PC1 (bottom) traces from an experimental session. Periods of sustained low (red) or high (blue) motor activity are indicated by shaded regions and transitions from low to high motor activity are delineated by green lines. Open blue boxes indicate high facial motion periods not included in analysis of sustained facial motor activity periods due to overlap with locomotion. **b**, Individual animal values and population means for high-frequency (30–100Hz) ECoG power for sustained low facial motion, high facial motion, and locomotion states. *indicates $p < 0.05$ for post-hoc LSD comparisons following a significant ($p < 0.05$) main effect of behavioral state in repeated measures ANOVA. **c**, Average spatial maps (n=6 mice) showing ACh3.0 (upper) and jRCaMP1b (lower) ΔF/F activity during three movement-defined sustained behavioral states. *indicates $p < 0.05$ for post-hoc LSD comparisons following a significant ($p < 0.05$) main effect of behavioral state in repeated measures ANOVA. **d**, ACh 3.0 amplitude in frontal-motor areas compared to visual areas during high facial motion. *indicates $p < 0.05$, paired t-test**. e**, Change in jRCaMP1b signal in frontal-motor and visual areas during treatment with scopolamine (0.5 mg/kg, i.p.; left) and mecamylamine (1 mg/kg, i.p.; right). The effect of each drug is shown as ΔF/F difference between drug and vehicle sessions within animal. * indicates $p < 0.05$ for one sample t-test within each brain region and paired t-test between brain regions.

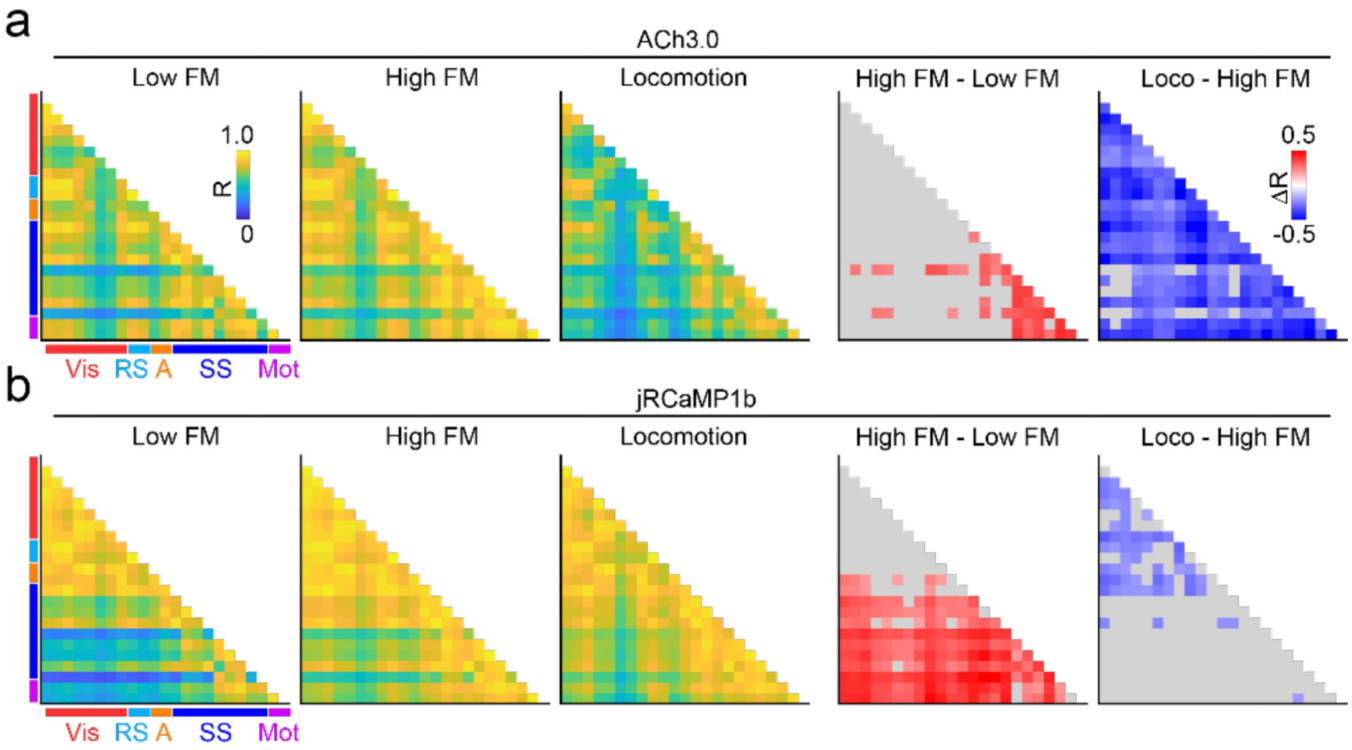

Figure 4. State-dependent variation in spatial correlations of cholinergic and neural activity.

a, Average peak cross-correlation matrices (n=6 mice) for cholinergic activity during three movement defined behavioral states: low facial motion, high facial motion, and locomotion, measured pairwise for CCFv3-defined cortical parcels in the left hemisphere (1st, 2nd, and 3rd columns). Average differences in correlation between high and low facial motion states (4th column) and between locomotion and high facial motion states (5th column) are shown for significant pairs (adjusted $p<0.01$, Benjamini-Yekutieli FDR corrected permutation test). Non-significant pairs are shown in gray. Vis, Visual; RS, retrosplenial; A, Auditory; SS, somatosensory; Mot, Motor. **b**, As in (a) for calcium (jRCaMP1b) activity.

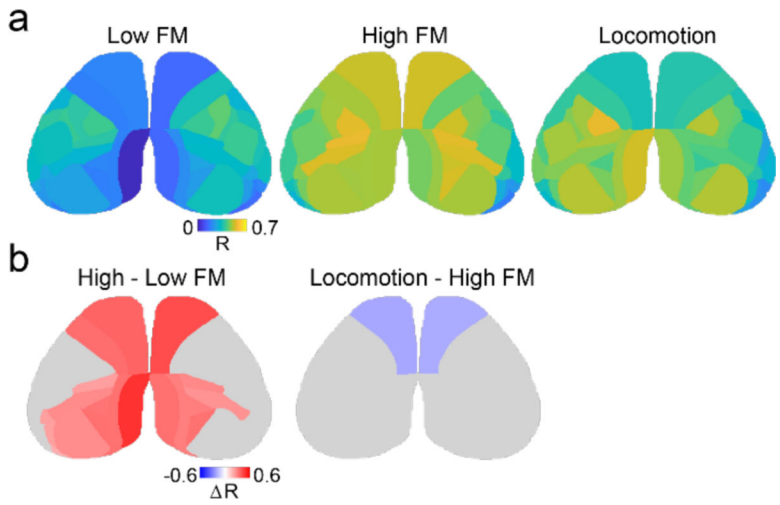

Figure 5. State-dependent spatial variation in correlations between cholinergic and calcium signals.

a, Average spatial maps (n=6 mice) showing peak cross-correlation coefficients between ACh3.0 and jRCaMP1b activity for each cortical parcel during three movement defined behavioral states: low facial motion, high facial motion, and locomotion. **b**. Average difference in correlation between high and low facial motion states (left) and between locomotion and high facial motion states (right) is shown for significant parcels (adjusted $p<0.01$, Benjamini-Yekutieli FDR corrected permutation test). Non-significant parcels are shown in gray.

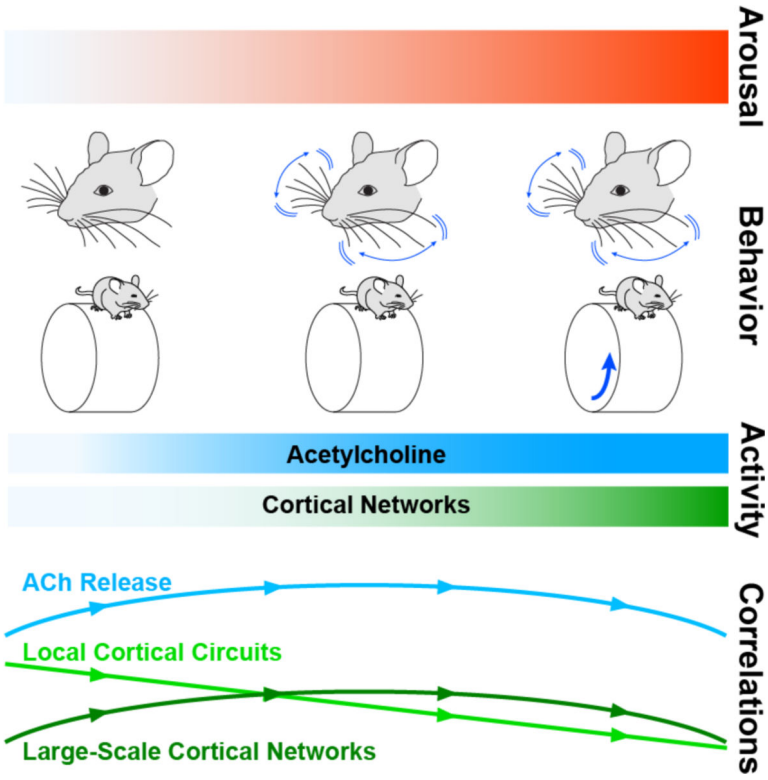

Figure 6. Relationship between arousal, cortical activity, and network synchrony.

Arousal is associated with distinct patterns of motor activity, marked by 1) elevated facial motion energy arising from movements of whiskers and facial muscles and 2) locomotion, which always co-occurs with facial movement. Increasing arousal corresponds to elevated neuronal activity and ACh release across the neocortex. With increased arousal, correlations within local cortical circuits measured via ECoG progressively decrease. In contrast, correlations within large-scale networks and of Ach release across the cortex measured with mesoscopic calcium imaging increase during moderate arousal associated with high facial motion energy but decrease with further increases in arousal with locomotion.